PHYSICAL REVIEW B **91**, 245155 (2015)

Phase transition in bulk single crystals and thin films of VO_2 by nanoscale infrared spectroscopy and imaging

Mengkun Liu,[1,2,*] Aaron J. Sternbach,[1] Martin Wagner,[1] Tetiana V. Slusar,[3] Tai Kong,[4] Sergey L. Bud'ko,[4] Salinporn Kittiwatanakul,[5] M. M. Qazilbash,[6] Alexander McLeod,[1] Zhe Fei,[1] Elsa Abreu,[7,8] Jingdi Zhang,[1,7] Michael Goldflam,[1] Siyuan Dai,[1] Guang-Xin Ni,[1] Jiwei Lu,[5] Hans A. Bechtel,[9] Michael C. Martin,[9] Markus B. Raschke,[10] Richard D. Averitt,[1] Stuart A. Wolf,[5,11] Hyun-Tak Kim,[3,12] Paul C. Canfield,[4] and D. N. Basov[1,†]

[1]*Department of Physics, The University of California at San Diego, La Jolla, California 92093, USA*

[2]*Department of Physics, Stony Brook University, Stony Brook, New York 11794, USA*

[3]*Metal-Insulator Transition Creative Research Center, ETRI, Daejeon 305-350, South Korea*

[4]*Ames Laboratory and Department of Physics and Astronomy, Iowa State University, Ames, Iowa 50010, USA*

[5]*Department of Materials Science and Engineering, University of Virginia, Charlottesville, Virginia 22904, USA*

[6]*Department of Physics, College of William & Mary, Williamsburg, Virginia 23187, USA*

[7]*Department of Physics, Boston University, Boston, Massachusetts 02215, USA*

[8]*Institute of Quantum Electronics, ETH Zurich, 8093 Zurich, Switzerland*

[9]*Advanced Light Source Division, Lawrence Berkeley National Laboratory, Berkeley, California 94720, USA*

[10]*Department of Physics, Department of Chemistry, and JILA, University of Colorado, Boulder, Colorado 80309, USA*

[11]*Department of Physics, University of Virginia, Charlottesville, Virginia 22904, USA*

[12]*School of Advanced Device Technology, Korean University of Science and Technology, Daejeon 305-333, South Korea*

(Received 21 January 2015; revised manuscript received 9 June 2015; published 29 June 2015)

We have systematically studied a variety of vanadium dioxide (VO_2) crystalline forms, including bulk single crystals and oriented thin films, using infrared (IR) near-field spectroscopic imaging techniques. By measuring the IR spectroscopic responses of electrons and phonons in VO_2 with sub-grain-size spatial resolution (~20 nm), we show that epitaxial strain in VO_2 thin films not only triggers spontaneous local phase separations, but also leads to intermediate electronic and lattice states that are intrinsically different from those found in bulk. Generalized rules of strain- and symmetry-dependent mesoscopic phase inhomogeneity are also discussed. These results set the stage for a comprehensive understanding of complex energy landscapes that may not be readily determined by macroscopic approaches.

DOI: 10.1103/PhysRevB.91.245155 PACS number(s): 72.80.Ga, 73.22.−f, 73.23.−b, 78.20.−e

I. INTRODUCTION

Transition metal oxides (TMOs) host an array of crystal forms, among which the material properties can vary dramatically. For example, the local energy landscape of electronic structures can vary from single crystals to polydomain films [1,2] or strain-engineered heterostructures [3]. In addition, the nontrivial charge and orbital orderings in TMOs are highly susceptible to local and external stimuli such as thermal excitation [4], strain [5–7], or light illumination [8–10]. The resultant phase transitions are often accompanied by inevitable mesoscopic electronic and/or magnetic inhomogeneities [11–14], making it extremely difficult to distinguish emergent single-phase properties from area-averaging phenomena originating from a mixed state [13,15–17]. As a result, experimental observations strongly depend on the particularities of the samples and measurement techniques, posing difficulties in interpreting the results obtained with complementary experimental approaches. Therefore a systematic investigation of one model TMO system within distinct crystalline states using one unique but versatile microscopic technique is imperative and can serve as a solid foothold for future research. Here we utilize infrared near-field methods to disentangle the *local* electron and lattice degrees of freedom in vanadium dioxide.

Vanadium dioxide (VO_2) is a canonical correlated electron TMO that has an insulator-to-metal transition with several orders of magnitude conductivity change accompanied by a first-order structural phase transition (monoclinic to rutile) at around 340 K [4]. Under almost six decades of intense studies, VO_2 has been fashioned into a diverse range of forms, such as bulk crystals [4,18,19], amorphous or highly oriented films [20–22], and nano-/microcrystals [23–27]. Although the growth of low-strain, freestanding single crystals is readily accomplished via solution growth [28,29], the growth of high-quality crystalline films has not been possible until recently with developments in epitaxial techniques [21,30]. Among these samples, the macroscopically measured metal-insulator transition (MIT) temperature T_{MIT} can vary by up to 100 K [20,22,29,31,32]. Their electronic and lattice properties also show distinct temperature dependences and anisotropic behaviors [20,26,33–37].

In this work, we are able to compare different crystal forms of this canonical phase transition material under identical test environments using systematic infrared near-field studies. The samples we investigated are solution-grown, freestanding, VO_2 single crystals and highly oriented epitaxial VO_2 films on TiO_2 substrates. We show that the global properties of these VO_2 samples arise from *a concerted interplay between self-organized phase inhomogeneity and strain-modified lattice and orbital reshuffling*.

*mengkun.liu@stonybrook.edu
†dbasov@physics.ucsd.edu

II. SCANNING NEAR-FIELD INFRARED MICROSCOPY AND SPECTROSCOPY

Scattering-type scanning near-field optical microscopy (s-SNOM) and Fourier transform IR nanospectroscopy (nano-IR) [38–41] are capable of performing IR nanoimaging as well as IR broadband nanospectroscopy. The surface topography, and electronic and phonon responses can be obtained simultaneously, a significant advantage over other types of nanoprobe techniques. It has been demonstrated as an extremely versatile tool for investigations of many different states of matter—from functional polymers [41,42], to two-dimensional materials [43] and meteorite composites [44]. Furthermore, its unique tip-sample interactions allow one to access and manipulate the photon momentum in addition to the photon energy [45], coupling new degrees of freedom to experiments with flexible probing schemes, as exemplified by recent investigations of thin crystals and interfacial effects [46,47].

Atomic force microscope (AFM)-based s-SNOM nanoimaging and broadband nano-IR spectroscopy have an optical spatial resolution limited, to first order, only by the AFM tip radius (∼20 nm). The key principle that enables these techniques is the demodulation of the tip-scattered signal at higher harmonics (S_n, $n \geqslant 2$) of the tip tapping frequency. In general, a demodulated signal at the second harmonic (S_2) is sufficient to achieve ∼20-nm resolution [48], while the near-field amplitude of higher harmonics such as S_3 and S_4 can register even better light confinement [49]. Therefore this procedure effectively discriminates the strongly localized near-field response from background far-field scattering with superior spatial resolution [38–40].

In this work we perform nanoimaging and nano-IR spectroscopy with different light sources to monitor the electronic phase transition and the lattice structural phase transition independently at representative spectral ranges. For mapping the electronic phase transition, we utilize a table-top quantum cascade laser (QCL) with frequency centered at ∼1000 cm^{-1}, enabling monochromatic IR imaging (as shown in Figs. 4–6 and Fig. 8 below). Since VO_2 reveals an energy gap of about 4000 cm^{-1}, IR imaging at 1000 cm^{-1} effectively probes the evolution of the Drude conductivity tail associated with the correlated electrons [14] (see also far-field optical conductivity curves in the Supplemental Material [50]). On the other hand, in order to register the phonon responses and hence effectively probe the local structural phase transition, we utilize synchrotron IR light from Beamline 5.4 of the Advanced Light Source (ALS) at Lawrence Berkeley National Lab to perform broadband infrared near-field spectroscopy (broadband nano-IR) (Fig. 7). The high brightness and broadband nature of the synchrotron source enables nano-IR spectroscopy that ranges from 450 to 4500 cm^{-1}, limited only by the detector and beamsplitter combination [51]. This spectral range allows us to address strain-reconfigured monoclinic phonon resonances at the nanoscale, probing the essential V-O bond deformation at ∼500–750 cm^{-1} with reduced mixed-phase ambiguity [52]. (The highest IR active phonon frequency in VO_2 reported by experiments and theory is ∼750 cm^{-1}) [26,50].

We attenuate the output power of the QCL to ∼5 mW, which yields a good enough signal-to-noise ratio for S_3- and S_4-based imaging (third and fourth harmonics of the modulated signal). For nano-IR with the broadband synchrotron source, the integrated infrared power (700–5000 cm^{-1}) is ∼0.5 mW, so that we obtain all the broadband nano-IR spectrum with second harmonic demodulation (S_2) [51].

III. SAMPLES

In this work, we examine low-strain, solution-grown bulk VO_2 crystals and highly oriented strained VO_2 films on $[001]_R TiO_2$ substrates. We also compare this work to our previous results on highly oriented VO_2 films on $[110]_R$ and $[100]_R$ TiO_2 substrates, and on low-strain polycrystalline VO_2 films on (r-cut) sapphire substrates. Despite the obvious variations in in-plane symmetry, these bulk crystals or films also possess dramatically different strain environments which lead to different MIT temperatures. In general, compressive (tensile) strain along c_R yields T_{MIT} lower (higher) than in bulk [22,35,36,53,54]. Bulk crystals (undoped) and polycrystalline films on sapphire substrates usually have a MIT close to 340 K. Films on $[001]_R TiO_2$ substrate have a compressive strain along c_R, leading to a $T_{MIT} < 340$ K [22,54]. Films on $[110]_R$ and $[100]_R$ TiO_2 substrates have a $T_{MIT} > 340$ K with local variations caused by strain inhomogeneities [35,36,55,56]. *It is important to point out that here* T_{MIT} *represents the global instead of the local M-I transition temperature, as discussed in our previous work* [55]. Different schemes have been suggested to explain the strain-induced T_{MIT} variation, including strong electronic correlations [57,58] and orbital control [35,54], but the microscopic mechanism behind the strain modulation remains unclear. Regarding the MIT in general, it is likely that both correlations and structural effects must be taken into account [10,59–61]. Independent of the precise microscopic mechanism, mesoscopic physics certainly is extremely important in these samples. As we will discuss in detail later, strain and symmetry are the two most important parameters for the mesoscopic pattern observed in VO_2. We first show the methods of sample fabrication below.

Bulk single crystals of VO_2 were grown out of a V_2O_5-rich binary melt using solution growth techniques [29,62]. Given the relatively low melting point of V_2O_5, combined with its low vapor pressure and the large, exposed, liquidus line for the formation of VO_2, VO_2 can be grown out of a solution of excess V_2O_5. For this work, roughly 8 g of V_2O_5 were placed in an amorphous silica tube with 1 g of lump VO_2 that had been synthesized by heating V_2O_5 under flowing N_2 gas. The V_2O_5 and VO_2 were carefully pumped and flushed with Ar gas with intermediate, gentle heating to encourage outgassing of any adsorbed gas. The silica tube was then sealed and heated to 1050 °C over 6 h, dwelled at 1050 °C for 3 h, and then slowly cooled to 775 °C over 50 or more hours. At this point the excess V_2O_5 was decanted from the rodlike VO_2 crystals by use of a centrifuge [29]. The single-crystalline rods grow along the high-temperature, rutile, c axis and have lengths of up to greater than 1 cm but have cross-sectional areas of less than 1 mm^2 (in some cases significantly smaller). Selected crystals are shown in the inset of Fig. 1. It should be noted that these crystals have experienced the minimum possible strain, given that they grew out of liquid and were removed from this liquid in the high-temperature state. When they cooled through the MIT

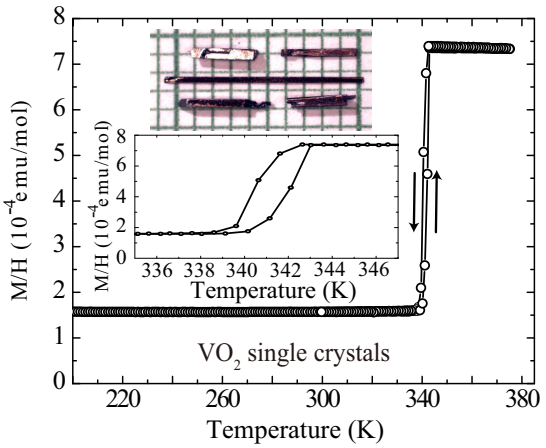

FIG. 1. (Color online) (a) Temperature-dependent dc magnetization susceptibility of bulk single-crystal VO_2. $T_{MIT} \approx 341 \pm 2$ K. (Inset) Top: microscopic image of selected VO_2 single crystals; bottom: magnetization curve expanded in the vicinity of the phase transition.

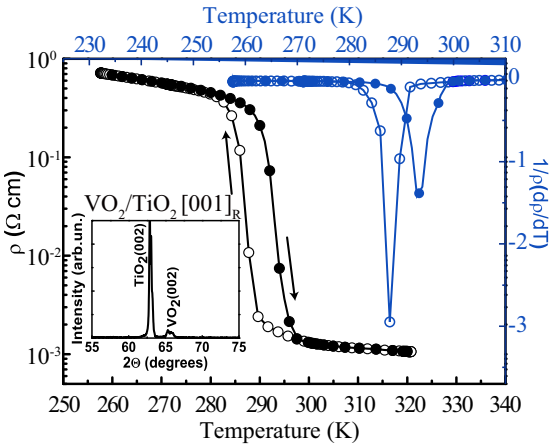

FIG. 2. (Color online) Temperature-dependent resistivity (black) and corresponding derivative (blue) curves for 30-nm VO_2/TiO_2 $[001]_R$ film. $T_{MIT} \approx 290 \pm 10$ K. Inset, x-ray diffraction intensity (arbitrary units). The solid and open circles represent temperature ramping up and down, respectively.

as they approached room temperature, they were freestanding in the growth ampule. The signature of the metal-to-insulator transition in these bulk single crystals can be seen clearly in the bulk dc magnetic susceptibility $M(T)/H$ data shown in Fig. 1. The phase transition is very sharp and manifests relatively little hysteresis for heating and cooling rates of roughly 0.2 K per minute. We avoid resistivity measurements here, since microcracks occurring during heating and cooling through the first-order M-I transition are a common drawback for transport measurements in bulk VO_2 crystals. When performing the near-field measurements, one end of the crystal is attached to the heating stage with a point contact, thereby minimizing sample-holder-induced strain.

The highly oriented VO_2 films on $[001]_R TiO_2$ substrate (c_R axis out of plane, see definition in Fig. 3) were fabricated by the pulsed-laser deposition method. A KrF excimer laser with a radiation wavelength of 248 nm was used to ablate the metallic vanadium target in an oxygen atmosphere. During thin-film deposition, the oxygen partial pressure was maintained at 14 mTorr and substrate temperature at 450 °C. The deposition rate of the films was about 0.5 nm/min. By adjusting the growth time, we have obtained films with different thicknesses. The temperature-dependent resistance of the ~30 nm VO_2/TiO_2 $[001]_R$ films are shown in Fig. 2. The maxima in $|\frac{1}{\rho}\frac{d\rho}{dT}|$ are broad and show substantial hysteresis. Based on this we can set a range for $T_{MIT} \approx 290 \pm 10$ K, with the understanding that this value suggests local, mesoscopic complexities and is not a "bulk value," as discussed later. X-ray characterization (inset of Fig. 2) is also performed, demonstrating the quality (i.e., highly oriented domains) of these films. VO_2 films on $[110]_R$ and $[100]_R$ TiO_2 substrates were grown by reactive-biased target ion-beam deposition [21] and have been previously studied and reported [35,36,55,56,63]. We compared all available films on TiO_2 substrates with the same orientations made from different deposition methods and obtained consistent results.

From the various samples investigated in this and previous studies [14,35,36,55,56], we conclude the following for VO_2.

(1) The MIT in VO_2 bulk crystals exhibits a sharp and well-defined phase boundary with $T_{MIT} \approx 341 \pm 2$ K. The hysteresis is narrow due to the minimum strain environment. (2) The MIT in VO_2/TiO_2 films with an out-of-plane c_R axis ($[001]_R$) is dominated by substrate-induced lattice clamping, revealing new structural and electronic ordering in a rather uniform manner. The substrate-induced compressive strain along c_R yields an isotropic $T_{MIT} < 340$ K and a wide hysteresis. (3) The MIT in VO_2/TiO_2 films with in-plane c_R axis ($[100]_R$ or $[110]_R$) is dominated by mesoscopic, anisotropic phase separation. Substrate-induced tensile strain along c_R leads to macroscopic electron transport anisotropy with $T_{MIT} > 340$ K when measured along c_R. ($T_{MIT} < 340$ K perpendicular to c_R). The thicknesses of all the thin films we investigated were greater than 30 nm (range from 30 to

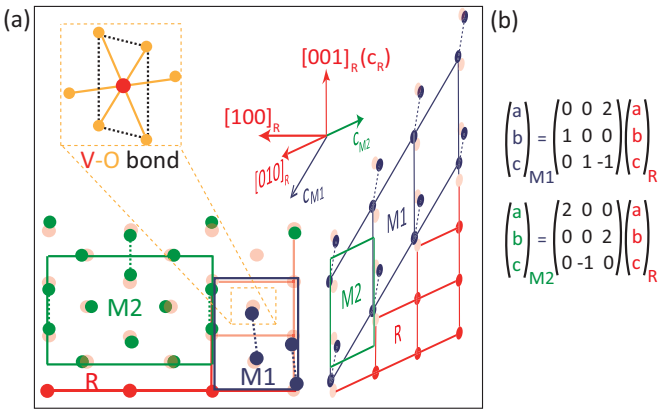

FIG. 3. (Color online) (a) Schematic of real-space lattice structures of monoclinic M1, M2, and rutile R phases. Blue (green) filled circles: vanadium atoms in M1 (M2) phase; red filled circles: vanadium atoms in R phase. Blue (green) solid line: unit cell of M1 (M2) phase. Blue (green) dashed line: V-V pairing in M1 (M2) phase. Red solid line: unit cell of R phase. The arrows indicate the corresponding lattice axes. (b) Matrix equation of M1-R, M2-R lattice relationship.

300 nm). Therefore, we cannot exclude the possibility that for much thinner films (e.g., a few nanometers) one could observe different microscopic patterns and strain-induced behaviors. For clarity we illustrate the lattice and unit cell structures of monoclinic M1, monoclinic M2, and rutile R phases in Fig. 3 [57,59,64,65]. In the M1 phase all V atoms pair and twist to form V-V dimers, while in the M2 phase half of the V atoms pair with the other half remaining unpaired [59]. The corresponding lattice axes are also shown in Fig. 3 as well. We note that our current characterization and categorization of the mesoscopic patterns in VO_2 are not exhaustive due to the diversity of crystal forms and to the current lower limit in IR frequency one can easily detect at the nanoscale ($>500\,cm^{-1}$).

IV. INFRARED NANOIMAGING OF VO_2 SINGLE CRYSTALS AND $VO_2/[001]_R$ TiO_2 FILMS

Figure 4 illustrates the distinct differences between bulk VO_2 crystals and highly oriented VO_2 film behavior, investigated by nano-IR imaging at $\sim$1000 cm^{-1}. For bulk crystals, there is an abrupt phase front that separates the different phases [Figs. 4(a)–4(f)]. From room temperature (RT) to $\sim$334 K the entire sample is in the M1 monoclinic insulating state [Fig. 4(a)]. Above 334 K, a striped monoclinic insulating M2 phase emerges and propagates from the bottom to the top of the field of view as the temperature increases, until at $\sim$336 K the entire sample ($\sim 30\,\mu m \times 100\,\mu m \times 3$ mm) becomes M2 [Figs. 4(b) and 4(c)]. At 339.96($\pm$0.03) K the metallic state emerges within the field of view of our nano-IR setup and it propagates relatively fast with very small temperature increments [Figs. 4(d) and 4(e)]. At 340.10($\pm$0.03) K the crystal becomes metallic within our field of view. At each temperature step we wait 10 min after the sample is fully equilibrated prior to the measurement. Figures 4(a)–4(f) clearly demonstrate that bulk crystals have well-defined phase boundaries that separate different states (see also Fig. S2 with enhanced contrast in the Supplemental Material [50]). The angle of the insulator-metal phase boundary is approximately 50 deg with respect to the c_R axis and can be affected by local impurities on the surface. We obtained essentially the same domain orientation at larger scales with an optical microscope as those reported in Refs. [66,67], where the bulk VO_2 samples were thermally excited by an electric current. Therefore the results of large-scale characterization of the single-crystal samples will not be covered in detail here. Our assignment of the M1 and M2 phase is confirmed by Raman spectroscopy (not shown) and further investigated with the broadband nano-IR studies shown in Fig. 7.

Figures 4(g)–4(l), on the other hand, show simultaneous near-field and AFM images of a 30-nm $VO_2/[001]_R$ TiO_2 film at room temperature. The near-field images are again measured at $\sim$1000 cm^{-1}. Due to an intrinsic topographic buckling [e.g., Fig. 4(h)], the films we used in this study are shaped into "microbeams" with different lateral widths, leading to various strain environments. In the vicinity of the buckling (or sometimes cracking) where the strain in the VO_2 film is effectively released, we found that for narrower beams the compressive epitaxial strain (along $[001]_R$) is overall reduced, leading to a higher local transition temperature, closer to 340 K. This is clearly identified in Fig. 4(g), where there are multiple

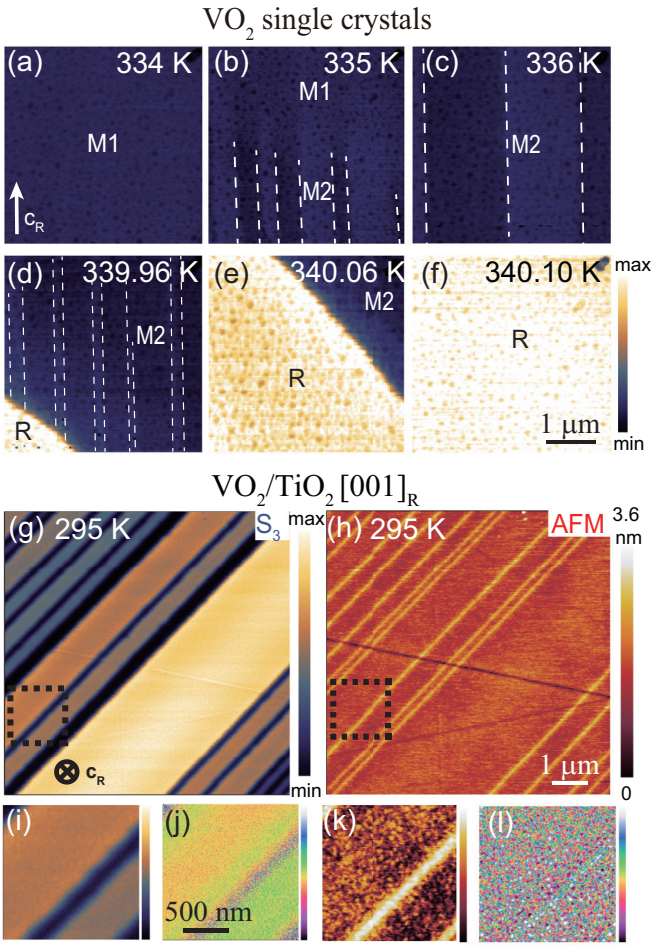

FIG. 4. (Color online) (a)–(f) IR scattering amplitude S_3 of VO_2 bulk single crystals acquired at different temperatures. Note that the temperature difference from (d) to (f) is only $\sim$0.14 K ($\pm$0.03 K). The stripes in the M2 phase are depicted by the white dashed lines. For enhanced contrast of (a)–(f) see Fig. S2 in Supplemental Materials [50]. (g),(h) simultaneously acquired scattering S_3 and AFM images of 30-nm VO_2/TiO_2 $[001]_R$ film. The dashed squares in (g) and (h) indicate the area whose expanded view is shown in (i)–(l): (i) near-field S_4 amplitude; (j) near-field S_4 phase; (k) AFM amplitude; and (l) AFM phase. The IR probing frequency (from a QCL laser) is 1000 cm^{-1}. The measurements for panels (g)–(l) are taken at 295 K.

scattered near-field signal levels reflecting steplike variations of IR conductivities between adjacent beams of different widths. The AFM amplitude (phase) in Fig. 4(k) [Fig. 4(l)] and the near-field amplitude (phase) in Fig. 4(i) [Fig. 4(j)] within the same microbeam are uniform and smooth, showing no mixture of "metallic" and "insulating" states within our 20-nm spatial resolution. It is unlikely that there is a depth-dependent conductivity variation since the film thickness is only $\sim$30 nm. This indicates that the variety of near-field signals observed in our VO_2 films [Fig. 4(g)] most likely originate from distinct stages of the MIT being stabilized in different domains of the film for a given temperature. We note that the microbeam width-dependent strain environment has been reported for $VO_2/TiO_2[100]_R$ films [55], in which the substrate provides an alternating local strain (along c_R) environment instead of

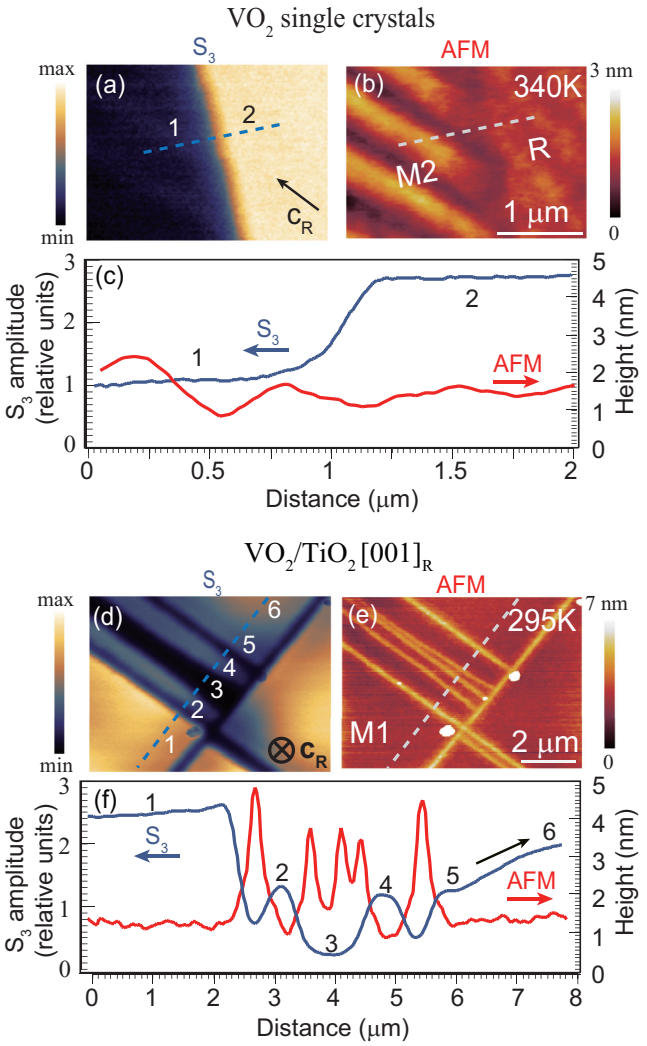

FIG. 5. (Color online) Near-field amplitude S_3 (a) and AFM (b) images of VO_2 bulk crystals at 340 K. (c) Line profiles of near-field amplitude S_3 (blue) and topography (red) taken along the dashed lines in (a) and (b), respectively. (d),(e) Near-field amplitude S_3 and AFM topography of 100-nm VO_2/TiO_2 $[001]_R$ film. The substrate induces a strain-dependent VO_2 metallicity. (f) Line profiles of the near-field amplitude S_3 (blue) and topography (red) taken along the dashed line in (d) and (e), respectively.

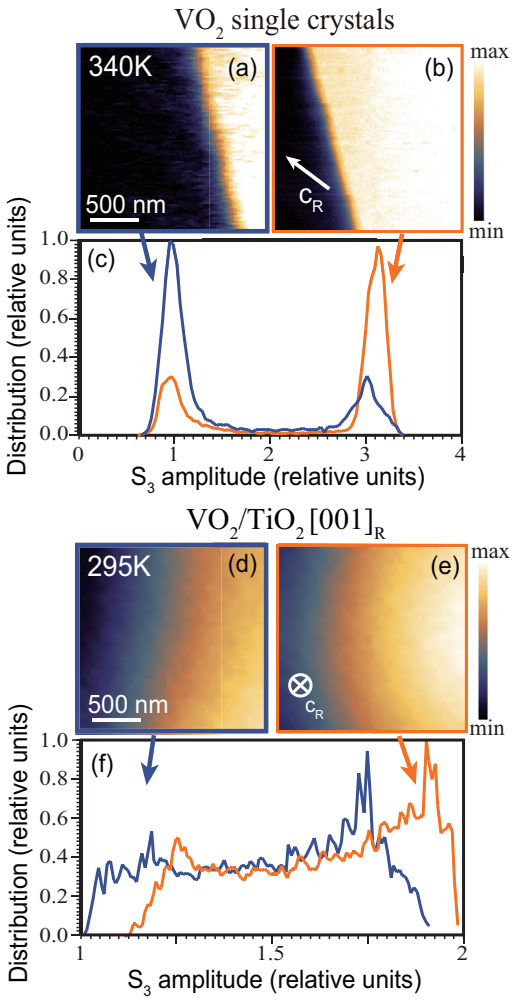

FIG. 6. (Color online) IR scattering amplitude (S_3) of VO_2 single crystals at (a) less-evolved and (b) more-evolved MIT regions at 340 K. (c) Histograms of (a) and (b) show a bimodal insulator–to-metal phase transition. In contrast, 100-nm VO_2/TiO_2 $[001]_R$ film at (d) less-strained and (e) more-strained regions of the film at 295 K exhibit a rather gradual and continuous MIT transition. The strain-relieved buckled edge is close to the left edge of Fig. 6(d) (not shown). (f) Histograms show gradual phase transitions spanning almost uniformly across the images, indicating a continuous evolution of the intermediate insulator-metallic states. All figures have the same scale. Scale bar: 500 nm.

an overall compressive strain mismatch, as is the case for VO_2/TiO_2 $[001]_R$ films.

To further illustrate the differences between bulk crystals and films on $[001]_R TiO_2$, we compare line profiles and histogram statistics of near-field IR signals in Figs. 5 and 6, respectively [68]. Line profiles of AFM topography and near-field amplitude S_3 of VO_2 bulk crystals reveal a sharp electronic as well as structural phase boundary with a width of the order of 100 nm [Figs. 5(a)–5(c)]. The insulating M2 state is observed with a reversible stripelike deformation in topography, in agreement with previous reports [53,69,70]. Line profiles of S_3 and topography in 100-nm-thick $VO_2/[001]_R$ TiO_2 films, however, reveal a terracelike or gradual change of VO_2 metallicity [Figs. 5(d)–5(f)]. Multiple near-field S_3 signal levels are clearly evident with a dependence on the strain environment, defined by the distance between buckles [$1 \rightarrow 6$ in Fig. 5(f)], in agreement with Fig. 4(g). Notice that at certain edges of the VO_2 beams the scattering signal can change continuously, indicating a gradual strain relief toward the edges or corners of the beams ($6 \rightarrow 5$). It is worth emphasizing the differences between the topography in bulk crystals and in VO_2/TiO_2 $[001]_R$ thin films. In bulk crystals the striped M2 phase [Figs. 3(a) and 3(b), and Figs. 5(a) and 5(b)] is reversible with temperature (the stripe will disappear with the M2 $\rightarrow$ M1 transition) and is spontaneously formed at $\sim$335 K. In contrast, the buckles in the particular VO_2 thin films [Figs. 4(g)–4(i), and Figs. 5(d) and 5(e)] we investigated were formed during the film deposition and are therefore permanent.

The histogram of the near-field amplitude S_3 gives a straightforward statistical representation of the metallicity at different stages of the phase transition for both samples

(Fig. 6). Bulk single crystals present binary statistics (in our case, dark blue or bright yellow in near-field contrast) everywhere on the samples, revealing that the samples are in either the fully insulating or the fully metallic state [Figs. 6(a)–6(c)]. However, the strained films can form a continuous gradient of scattering signals over the sample. In Figs. 6(d)–6(e) we measured at two adjacent locations close to a strain-relieved edge [to the left of Fig. 6(d), not shown] in the 100-nm VO_2/TiO_2 $[001]_R$ film. The continuous histograms in this case clearly reveal an evolution of the intermediate metallic state that advances toward a fully metallic state under high epitaxial strain.

V. BROADBAND NANO-IR OF VO_2 SINGLE CRYSTALS AND $VO_2/[001]_R$ TiO_2 FILMS

To carefully map out the subtle changes in lattice and electronic states among our samples at the nano- and mesoscopic scales, we rely on the spectroscopic signatures that are representative of the structural and electronic properties. Broadband nano-IR experiments with a lateral spatial resolution below 20 nm were performed at ALS for the bulk crystals and thin films. The IR active phonon responses of the M1 and M2 phases are taken at three adjacent locations across the M1-M2 interface in the single crystal at 337 K [see topography in Fig. 7(a)], and the spectral amplitude [51] is plotted in Fig. 7(b). When going through the M1 to M2 phase transition, VO_2 is known to acquire a slight tensile strain along the c_R axis [71] [see also the phase diagram in Fig. 8(a)]. Accordingly, we observe a blue shift of the ~520-cm^{-1} phonon peak. The peak positions corresponding to the phonon response of M1 are consistent with previous experimental work reporting A_u phonons at ~521, ~607, and ~637 cm^{-1} [26,52]. We also report here a pure M2 phonon response, which shows significant difference. While single crystals are often regarded as classical strain-free samples and we have indeed made great efforts to grow them in a strain-free environment, the M1 phase (strain free) and M2 phase (strained) can nevertheless coexist under ambient conditions, generating complexities in terms of the spontaneous phase inhomogeneities (striped M2 state). We expect this self-organized strain environment to be more complicated for highly doped single crystals [29] and crystals under uniaxial stress [57,72] or high hydrodynamic pressure [72,73], since several different monoclinic states (M1, M2, T) can coexist. This could be the reason why there are ambiguous "two-phase" regions observed in early experiments on bulk crystal VO_2 crystals [19].

In VO_2/TiO_2 $[001]_R$ films, the spectroscopic transition from M1 insulator to rutile metal is clearly demonstrated as

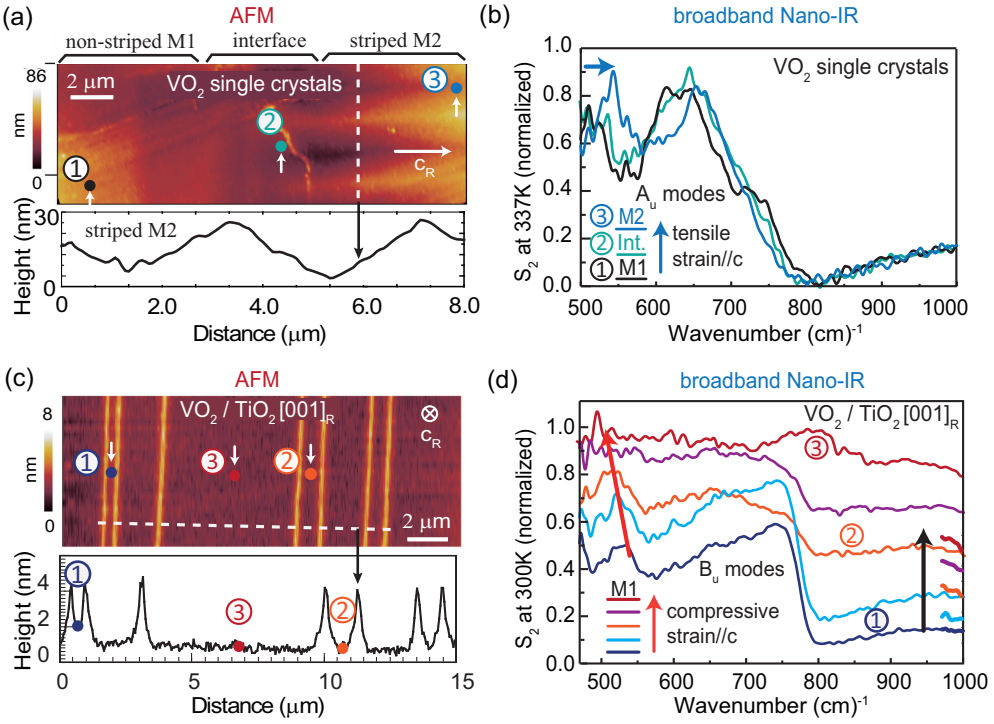

FIG. 7. (Color online) (a) Top: AFM topography of an M1-M2 interface in VO_2 single crystal at 337 K; bottom: AFM line scan of the striped M2 phase (along the white dashed line in the top panel). (b) Normalized nano-IR spectra S_2 at different locations corresponding to the spots indicated by the short white arrows in Fig. 7(a). Since the c_R axis is in plane [white horizontal arrow in Fig. 7(a)], the major contribution of the signal is from A_u phonon modes ($E//a_R$). (c) Top: AFM topography of the 100-nm VO_2/TiO_2 $[001]_R$ film at room temperature. Bottom: AFM line scans of the buckles and the microbeams (along white dashed line in the top panel). (d) Normalized nano-IR spectra S_2 taken at the center of the microbeams with different beam widths. Three out of the five representative spectra are taken at the probe spots indicated by the short white arrows in (c). Since the c_R axis is out of plane, the major contribution of the signal is from B_u phonon modes. For clarity, the curves in (d) are shifted vertically. The original positions of each curve are indicated at the high-frequency end of the same panel. We note that since the tip-scattered IR wave vector and its polarization is not well defined, the assignments of A_u and B_u modes in (b) and (d) are qualitative. We also note that all the S_2 spectra shown in Figs. 7(b) and 7(d) have a ~20-nm spatial resolution.

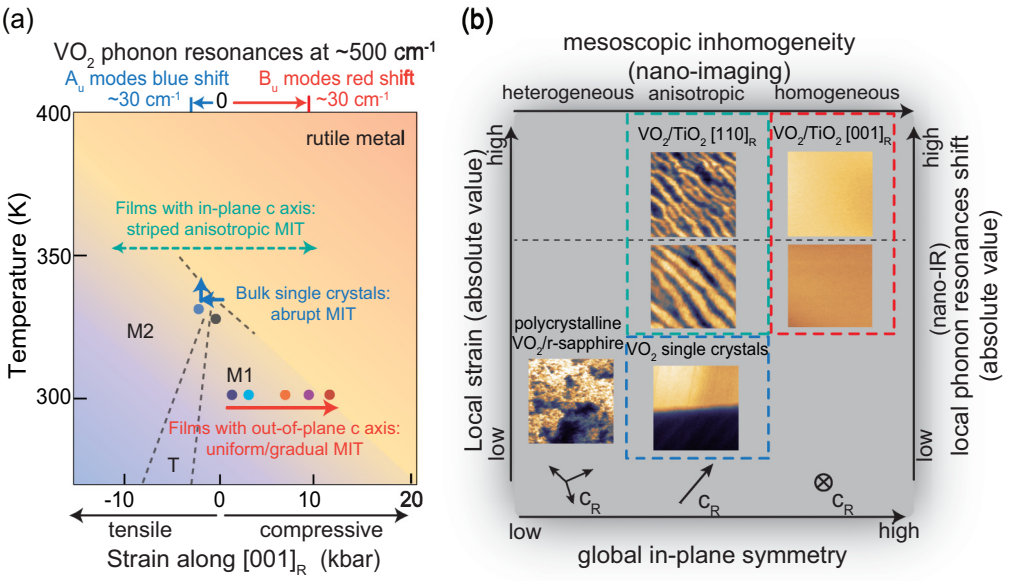

FIG. 8. (Color online) (a) VO_2 temperature-strain phase diagram. The vertical position of the arrows indicates the global T_{MIT} of corresponding VO_2 samples. The horizontal span of the arrows indicates the extent of the strain environment in the samples. The phonon resonance blueshifts in single crystals and redshifts in films with out-of-plane c_R axis, with increasing tensile and compressive strain along c_R, respectively, as indicated at the top of Fig. 8(a). The films are referring to VO_2 films on TiO_2 substrates. (b) Generalized strain-symmetry-inhomogeneity trends of VO_2 crystals and films. With increasing global in-plane symmetry (see text), the mesoscopic patterns probed by nanoimaging become more homogeneous (heterogeneous → anisotropic → homogeneous). With increasing local strain, the periodicity of the stripelike pattern (in the case of VO_2/TiO_2 $[110]_R$ [36,55]) or strain-induced metallicity (in the case of VO_2/TiO_2 $[001]_R$) changes accordingly. The phonon resonance shift probed by broadband nano-IR is a good indicator of the local strain which modifies the lattice structure. Bottom left panel: 100-nm VO_2/r sapphire at 343 K; top middle: 50-nm VO_2/TiO_2 $[110]_R$ at 340 K (higher local strain); middle: 100-nm VO_2/TiO_2 $[110]_R$ at 332 K (lower local strain); bottom middle: VO_2 single crystal at 340 K; top right: 100-nm VO_2/TiO_2 $[001]_R$ at 300 K (selected scan window far away from buckles, higher local strain); middle right: 100-nm VO_2/TiO_2 $[001]_R$ at 300 K (selected scan window closer to buckles, lower local strain). All images in (b) are 3 × 3 mm taken with near-field amplitude S_3, except for VO_2 on sapphire (S_2).

a gradual evolution in both electronic and lattice response [Fig. 7(d)]. The broadband nano-IR scans are performed at the center of the microbeams with different beam widths (at room temperature), yielding different strain environments. The locations of representative probe spots (three out of five) with ~20-nm resolution are indicated in Fig. 7(c). With increasing compressive strain (wider beam width) along c_R, the M1 phonon response at ~540 cm^{-1} (B_u mode) gradually redshifts, as indicated by the red arrow in Fig. 7(d). At the same time, the metallicity also gradually increases, as indicated by the black arrow at ~950 cm^{-1}. We note that we observe another B_u mode at ~750 cm^{-1}, whose magnitude decreases with strain but whose frequency shift shows no consistent behavior. In this work we focus on the ~540 cm^{-1} resonance. The strain levels for each the microbeams we investigated with broadband nano-IR are roughly estimated in the VO_2 phase diagram of Fig. 8(a), as will be discussed later. We note that the curves in Fig. 7(d) are vertically shifted for clarity and that the original positions of each curve are indicated in the ~960–1000 cm^{-1} range. Since the ~540 cm^{-1} monoclinic phonon reflects the V-O bond length, the prominent redshift is in agreement with previous experiments which suggested that V-O bond lengths are increased under compressive strain along c_R [54]. The increasing metallicity is also in line with the statement that orbital occupancies are dramatically altered under strain [35,54]. The results of Figs. 7(c) and 7(d) indicate that strain tuning and the corresponding lattice and electronic responses can be gradual, revealing intrinsic pure phase properties and ruling out ambiguous averaging effects within our spatial resolution.

VI. SUMMARY OF MESOSCOPIC INHOMOGENEITY IN VO_2 SINGLE CRYSTALS AND VO_2 FILMS ON FOUR DIFFERENT SUBSTRATES

To illustrate the strain environment and corresponding phase transitions in all of the samples, we map each sample onto the phase diagram in Fig. 8(a). Bulk crystals have the narrowest strain span (blue horizontal arrow) indicated by a sharp MIT at around 340 K (Figs. 1 and 2). VO_2 films on $[001]_R TiO_2$ have a compressive strain along c_R that can lead to a continuous redshift of the phonon response and increase in the IR conductivity (red arrow). The colored dots correspond to the estimated strain environment at which the broadband nano-IR data are taken in Fig. 7. We would like to emphasize that our spatial resolution is sufficient to report on single-phase properties. That is, each dot on the phase diagram corresponds to a new structural or orbital state and there is no "mixed-phase" signal. For comparison, we also illustrate the strain environment in samples with the c_R axis in plane, e.g., samples on $[100]_R$ and $[110]_R$ TiO_2 substrates, as previously studied (green dashed double arrow) [36,55]. For these samples, an anisotropic stripe state is induced with alternating tensile and compressive strain [see also Fig. 8(b)]

[36,56]. As a result, a combination of phase separation and strain-induced modification of orbital occupancy is expected to play a very important role in these films.

Figure 8(b) sums up the representative mesoscopic domain textures in some of the VO_2 samples we measured. For VO_2 bulk crystals (blue panel), a sharp insulator-to-metal phase boundary is observed between the M and R phases. For highly oriented VO_2 films on $[110]_R$ TiO_2 with in-plane c_R axis (green panels), self-organized patterns are evident. In these films, an alternation of compressive and tensile strain yields interesting stripelike patterns due to the epitaxial strain mismatch and VO_2 symmetry breaking [36,55]. For highly oriented VO_2/TiO_2 $[001]_R$ films with an out-of-plane c_R axis (red panel), we observe a gradual phase transition with temperature, as detailed in this study. No stripelike pattern is observed. For comparison, we also include previously reported results for VO_2 films on r-cut sapphire substrates [74], where the samples can have several preferred growth directions due to large lattice mismatch.

While the near-field images in Fig. 8(b) reveal the substantial phase complexity of VO_2, we have nevertheless been able to identify distinct trends that assist in understanding the mesoscopic inhomogeneity observed with nanoimaging and broadband nano-IR. These trends are summarized in the x- and y-axes in Fig. 8(b) and described using global in-plane symmetry and local strain parameters. For clarity, we first introduce the notion of global in-plane symmetry [bottom x axis of Fig. 8(b)]. Global in-plane symmetry includes both the crystal symmetry of the sample and the orientation of the substrate. It changes with different substrates or with different film orientations, even though the film is always composed of the same material. For example, for VO_2 films on r-cut sapphire substrates [lower left panel in Fig. 8(b)], the films have several in-plane c_R orientations (low symmetry) due to lattice symmetry mismatch between the sample and the substrate. This results in phase percolation without clear mesoscopic patterns (heterogeneous). Highly oriented films with one specific in-plane c_R axis (intermediate symmetry) yields stripelike (anisotropic) patterns (for example, VO_2/TiO_2 $[110]_R$ in Fig. 8(b), top middle panel) [36,56] and can have spontaneous symmetry breaking defined by the crystal axis of the VO_2 films [55]. For films with the c_R axis out of plane (highest in-plane symmetry), the mesoscopic response is rather uniform (homogenous; for example, VO_2/TiO_2 $[001]_R$, top right panel). Besides in-plane symmetry, one should also consider local strain [left y axis in Fig. 8(b)], which is distinct from hydrostatic pressure applied to the samples. Local strain is related to the global film-substrate symmetry due to corresponding strain mismatch but can also be adjusted independently through, for example, film thickness and strain relief due to buckles, cracks, or defects. It changes the intrinsic structural and electronic configurations (e.g., VO_2/TiO_2 $[001]_R$, top right panel, and Ref. [54]) while also resulting in a spatial phase redistribution so as to minimize the local strain energy. (For example, VO_2/TiO_2 $[110]_R$, top middle panel; notice that strain decreases with increasing film thickness and that the mesoscopic stripe periodicity is therefore scaled accordingly.)

VII. SUMMARY AND OUTLOOK

In conclusion, phase separation and structural and electronic reconfigurations can occur concertedly in vanadium dioxide, controlled by the local strain and global symmetry. Our results are specific to VO_2 yet universally relatable to other correlated electron materials [75]. Previously studied VO_2 nanobeams and microcrystals can be regarded as specific cases with some of the unique strain environments identified in the present study [23–25,76]. In future studies, ultrafast femtosecond dynamics [77–79] and magnetic orders [1] can also be included in systematic near-field investigations of TMOs, which will lead to a better understanding of the rich diversity of mesoscopic and microscopic phenomena at fundamental time and length scales in materials such as manganites and high-temperature superconductors.

ACKNOWLEDGMENTS

D.N.B. acknowledges support from ARO under Grant No. W911NF-13-1-0210. M.L. and M.G. acknowledge support from Helmholtz Virtual Institute MEMRIOX. Development of nano-optics capabilities at UCSD is supported by DOE-BES under Grant No. DE-SC0012592. R.D.A. and E.A. acknowledge support from DOE-BES under Grant No. DE-FG02-09ER46643. A.S.M. acknowledges support from the Basic Energy Sciences initiative of the U.S. Department of Energy (DOE-BES). The Advanced Light Source is supported by the Director, Office of Science, Office of Basic Energy Sciences, of the U.S. Department of Energy under Contract No. DE-AC02-05CH11231. P.C.C., S.L.B., and T.K. acknowledge support from the U.S. Department of Energy, Office of Basic Energy Science, Division of Materials Sciences and Engineering for the research performed at the Ames Laboratory. Ames Laboratory is operated for the U.S. Department of Energy by Iowa State University under Contract No. DE-AC02-07CH11358. H.T.K. acknowledges support from the creative project in ETRI. S.K., J.L., and S.A.W. are grateful for support from the Nanoelectronics Research Initiative (NRI) and VMEC. M.M.Q. acknowledges support from NSF DMR (Grant No. 1255156) and the Jeffress Memorial Trust. We acknowledge Rob Olmon for valuable discussions and thank him for developing synchrotron infrared near-field spectroscopy (SINS) at the ALS.

[1] E. Dagotto, *Nanoscale Phase Separation and Colossal Magnetoresistance*, Springer Series in Solid-State Sciences (Springer, New York, 2002).

[2] V. Lyahovitskaya, Y. Feldman, I. Zon, E. Wachtel, I. Lubomirsky, and A. L. Roytburd, Adv. Mater. **17**, 1956 (2005).

[3] H. Y. Hwang, Y. Iwasa, M. Kawasaki, B. Keimer, N. Nagaosa, and Y. Tokura, Nat. Mater. **11**, 103 (2012).

[4] F. J. Morin, Phys. Rev. Lett. **3**, 34 (1959).

[5] J. Locquet, J. Perret, and J. Fompeyrine, Nature (London) **394**, 453 (1998).

[6] J. Wang, J. B. Neaton, H. Zheng, V. Nagarajan, S. B. Ogale, B. Liu, D. Viehland, V. Vaithyanathan, D. G. Schlom, U. V Waghmare, N. A. Spaldin, K. M. Rabe, M. Wuttig, and R. Ramesh, Science **299**, 1719 (2003).

[7] J. Cao and J. Wu, Mater. Sci. Eng., R **71**, 35 (2011).

[8] D. Fausti, R. I. Tobey, N. Dean, S. Kaiser, A. Dienst, M. C. Hoffmann, S. Pyon, T. Takayama, H. Takagi, and A. Cavalleri, Science **331**, 189 (2011).

[9] M. Liu, H. Y. Hwang, H. Tao, A. C. Strikwerda, K. Fan, G. R. Keiser, A. J. Sternbach, K. G. West, S. Kittiwatanakul, J. Lu, S. A. Wolf, F. G. Omenetto, X. Zhang, K. A. Nelson, and R. D. Averitt, Nature (London) **487**, 345 (2012).

[10] D. N. Basov, R. D. Averitt, D. van der Marel, M. Dressel, and K. Haule, Rev. Mod. Phys. **83**, 471 (2011).

[11] E. Dagotto, T. Hotta, and A. Moreo, Phys. Rep. **344**, 1 (2001).

[12] J. A. Krumhansl, J. Phys. IV **05**, C2 (1995).

[13] K. Lai, M. Nakamura, W. Kundhikanjana, M. Kawasaki, Y. Tokura, M. A. Kelly, and Z.-X. Shen, Science **329**, 190 (2010).

[14] M. M. Qazilbash, M. Brehm, B.-G. Chae, P.-C. Ho, G. O. Andreev, B.-J. Kim, S. J. Yun, A. V. Balatsky, M. B. Maple, F. Keilmann, H.-T. Kim, and D. N. Basov, Science **318**, 1750 (2007).

[15] T. Becker, C. Streng, Y. Luo, V. Moshnyaga, B. Damaschke, N. Shannon, and K. Samwer, Phys. Rev. Lett. **89**, 237203 (2002).

[16] R. J. Zeches, M. D. Rossell, J. X. Zhang, A. J. Hatt, Q. He, C.-H. Yang, A. Kumar, C. H. Wang, A. Melville, C. Adamo, G. Sheng, Y.-H. Chu, J. F. Ihlefeld, R. Erni, C. Ederer, V. Gopalan, L. Q. Chen, D. G. Schlom, N. A. Spaldin, L. W. Martin, and R. Ramesh, Science **326**, 977 (2009).

[17] M. K. Stewart, J. Liu, M. Kareev, J. Chakhalian, and D. N. Basov, Phys. Rev. Lett. **107**, 176401 (2011).

[18] J. B. Goodenough, Annu. Rev. Mater. Sci. **1**, 101 (1971).

[19] J. B. Goodenough, J. Solid State Chem. **3**, 490 (1971).

[20] J. Lu, K. G. West, and S. A. Wolf, Appl. Phys. Lett. **93**, 262107 (2008).

[21] K. G. West, J. Lu, J. Yu, D. Kirkwood, W. Chen, Y. Pei, J. Claassen, and S. A. Wolf, J. Vac. Sci. Technol. A **26**, 133 (2008).

[22] Y. Muraoka and Z. Hiroi, Appl. Phys. Lett. **80**, 583 (2002).

[23] J. Wu, Q. Gu, B. S. Guiton, N. P. De Leon, L. Ouyang, and H. Park, Nano Lett. **6**, 2313 (2006).

[24] J. Cao, E. Ertekin, V. Srinivasan, W. Fan, S. Huang, H. Zheng, J. W. L. Yim, D. R. Khanal, D. F. Ogletree, J. C. Grossman, and J. Wu, Nat. Nanotechnol. **4**, 732 (2009).

[25] A. Tselev, E. Strelcov, I. A. Luk'yanchuk, J. D. Budai, J. Z. Tischler, I. N. Ivanov, K. Jones, R. Proksch, S. V Kalinin, and A. Kolmakov, Nano Lett. **10**, 2003 (2010).

[26] T. J. Huffman, P. Xu, M. M. Qazilbash, E. J. Walter, H. Krakauer, J. Wei, D. H. Cobden, H. A. Bechtel, M. C. Martin, G. L. Carr, and D. N. Basov, Phys. Rev. B **87**, 115121 (2013).

[27] X. He, T. Xu, X. Xu, Y. Zeng, J. Xu, L. Sun, C. Wang, H. Xing, B. Wu, A. Lu, D. Liu, X. Chen, and J. Chu, Sci. Rep. **4**, 6544 (2014).

[28] P. B. Allen, R. M. Wentzcovitch, W. W. Schulz, and P. C. Canfield, Phys. Rev. B **48**, 4359 (1993).

[29] T. Kong, M. W. Masters, S. L. Bud'ko, and P. C. Canfield, APL Mat. **3**, 041502 (2015).

[30] B.-J. Kim, Y. W. Lee, S. Choi, B.-G. Chae, and H.-T. Kim, J. Korean Phys. Soc. **50**, 653 (2007).

[31] S. Kittiwatanakul, J. Lu, and S. A. Wolf, Appl. Phys. Exp. **4**, 091104 (2011).

[32] S. Kittiwatanakul, S. A. Wolf, and J. Lu, Appl. Phys. Lett. **105**, 073112 (2014).

[33] C. Everhart and J. MacChesney, J. Appl. Phys. **39**, 2872 (1968).

[34] P. Bongers, Solid State Commun. **3**, 275 (1965).

[35] E. Abreu, M. Liu, J. Lu, K. G. West, S. Kittiwatanakul, W. Yin, S. A. Wolf, and R. D. Averitt, New J. Phys. **14**, 083026 (2012).

[36] M. K. Liu, M. Wagner, E. Abreu, S. Kittiwatanakul, A. McLeod, Z. Fei, M. Goldflam, S. Dai, M. M. Fogler, J. Lu, S. A. Wolf, R. D. Averitt, and D. N. Basov, Phys. Rev. Lett. **111**, 096602 (2013).

[37] X. Zhong, P. LeClair, S. K. Sarker, and A. Gupta, Phys. Rev. B **86**, 094114 (2012).

[38] S. Amarie, T. Ganz, and F. Keilmann, Opt. Express **17**, 21794 (2009).

[39] F. Keilmann, A. J. Huber, and R. Hillenbrand, J. Infrared Milli., Terahz. Waves **30**, 1255 (2009).

[40] D. Bonnell, D. Basov, M. Bode, U. Diebold, S. Kalinin, V. Madhavan, L. Novotny, M. Salmeron, U. Schwarz, and P. Weiss, Rev. Mod. Phys. **84**, 1343 (2012).

[41] J. M. Atkin, S. Berweger, A. C. Jones, and M. B. Raschke, Adv. Phys. **61**, 745 (2012).

[42] B. Knoll and F. Keilmann, Nature (London) **399**, 134 (1999).

[43] D. N. Basov, M. M. Fogler, A. Lanzara, F. Wang, and Y. Zhang, Rev. Mod. Phys. **86**, 959 (2014).

[44] G. Dominguez, A. S. Mcleod, Z. Gainsforth, P. Kelly, H. A. Bechtel, F. Keilmann, A. Westphal, M. Thiemens, and D. N. Basov, Nat. Commun. **5**, 5445 (2014).

[45] Z. Fei, G. O. Andreev, W. Bao, L. M. Zhang, A. S. McLeod, C. Wang, M. K. Stewart, Z. Zhao, G. Dominguez, M. Thiemens, M. M. Fogler, M. J. Tauber, A. H. Castro-Neto, C. N. Lau, F. Keilmann, and D. N. Basov, Nano Lett. **11**, 4701 (2011).

[46] Z. Fei, A. S. Rodin, G. O. Andreev, W. Bao, A. S. McLeod, M. Wagner, L. M. Zhang, Z. Zhao, M. Thiemens, G. Dominguez, M. M. Fogler, A. H. Castro Neto, C. N. Lau, F. Keilmann, and D. N. Basov, Nature **487**, 82 (2012).

[47] S. Dai, Z. Fei, Q. Ma, A. S. Rodin, M. Wagner, A. S. McLeod, M. K. Liu, W. Gannett, W. Regan, K. Watanabe, T. Taniguchi, M. Thiemens, G. Dominguez, A. H. Castro Neto, A. Zettl, F. Keilmann, P. Jarillo-Herrero, M. M. Fogler, and D. N. Basov, Science **343**, 1125 (2014).

[48] T. Taubner, R. Hillenbrand, and F. Keilmann, J. Microsc. **210**, 311 (2003).

[49] F. Huth, A. Chuvilin, M. Schnell, I. Amenabar, R. Krutokhvostov, S. Lopatin, and R. Hillenbrand, Nano Lett. **13**, 1065 (2013).

[50] See Supplemental Material at http://link.aps.org/supplemental/10.1103/PhysRevB.91.245155 for far-field optical conductivity measurements on VO_2/sapphire and enhanced images of M1, M2, and R phases.

[51] H. A. Bechtel, E. A. Muller, R. L. Olmon, M. C. Martin, and M. B. Raschke, Proc. Natl. Acad. Sci. USA **111**, 7191 (2014).

[52] W. W. Peng, G. Niu, R. Tétot, B. Vilquin, F. Raimondi, J. B. Brubach, E. Amzallag, T. Yanagida, S. Autier-Laurent, P. Lecoeur, and P. Roy, J. Phys.: Condens. Matter **25**, 445402 (2013).

[53] A. Tselev, V. Meunier, E. Strelcov, W. A. Shelton, I. A. Luk'yanchuk, K. Jones, R. Proksch, A. Kolmakov, and S. V Kalinin, ACS Nano **4**, 4412 (2010).

[54] N. B. Aetukuri, A. X. Gray, M. Drouard, M. Cossale, L. Gao, A. H. Reid, R. Kukreja, H. Ohldag, C. A. Jenkins, E. Arenholz, K. P. Roche, H. A. Dürr, M. G. Samant, and S. S. P. Parkin, Nat. Phys. **9**, 661 (2013).
[55] M. Liu, M. Wagner, J. Zhang, A. McLeod, S. Kittiwatanakul, Z. Fei, E. Abreu, M. Goldflam, A. J. Sternbach, S. Dai, K. G. West, J. Lu, S. A. Wolf, R. D. Averitt, and D. N. Basov, Appl. Phys. Lett. **104**, 121905 (2014).
[56] J. Laverock, S. Kittiwatanakul, A. A. Zakharov, Y. R. Niu, B. Chen, S. A. Wolf, J. W. Lu, and K. E. Smith, Phys. Rev. Lett. **113**, 216402 (2014).
[57] J. Pouget, H. Launois, J. D'Haenens, P. Merenda, and T. Rice, Phys. Rev. Lett. **35**, 873 (1975).
[58] B. Lazarovits, K. Kim, K. Haule, and G. Kotliar, Phys. Rev. B **81**, 115117 (2010).
[59] J. P. Pouget, H. Launois, T. M. Rice, P. Dernier, A. Gossard, G. Villeneuve, and P. Hagenmuller, Phys. Rev. B **10**, 1801 (1974).
[60] R. M. Wentzcovitch, W. W. Schulz, and P. B. Allen, Phys. Rev. Lett. **72**, 3389 (1994).
[61] J. D. Budai, J. Hong, M. E. Manley, E. D. Specht, C. W. Li, J. Z. Tischler, D. L. Abernathy, A. H. Said, B. M. Leu, L. A. Boatner, R. J. Mcqueeney, and O. Delaire, Nature (London) **515**, 535 (2014).
[62] P. Canfield and Z. Fisk, Philos. Mag. B **65**, 1117 (1992).
[63] J. Laverock, A. R. H. Preston, D. Newby, Jr., K. E. Smith, S. Sallis, L. F. J. Piper, S. Kittiwatanakul, J. W. Lu, S. A. Wolf, M. Leandersson, and T. Balasubramanian, Phys. Rev. B **86**, 195124 (2012).
[64] M. Marezio, D. McWhan, J. Remeika, and P. Dernier, Phys. Rev. B **5**, 2541 (1972).
[65] Y. Ji, Y. Zhang, M. Gao, Z. Yuan, Y. Xia, C. Jin, B. Tao, C. Chen, Q. Jia, and Y. Lin, Sci. Rep. **4**, 4854 (2014).
[66] B. Fisher, J. Phys. C: Solid State Phys. **8**, 2072 (1975).
[67] B. Fisher, J. Phys. C: Solid State Phys. **9**, 1201 (1976).
[68] M. M. Qazilbash, M. Brehm, G. O. Andreev, A. Frenzel, P. C. Ho, B.-G. Chae, B.-J. Kim, S. J. Yun, H.-T. Kim, A. V Balatsky, O. G. Shpyrko, M. B. Maple, F. Keilmann, and D. N. Basov, Phys. Rev. B **79**, 075107 (2009).
[69] J. M. Atkin, S. Berweger, E. K. Chavez, M. B. Raschke, J. Cao, W. Fan, and J. Wu, Phys. Rev. B **85**, 020101(R) (2012).
[70] E. Strelcov, A. Tselev, I. Ivanov, J. D. Budai, J. Zhang, J. Z. Tischler, I. Kravchenko, S. V Kalinin, and A. Kolmakov, Nano Lett. **12**, 6198 (2012).
[71] J. H. Park, J. M. Coy, T. S. Kasirga, C. Huang, Z. Fei, S. Hunter, and D. H. Cobden, Nature (London) **500**, 431 (2013).
[72] L. A. Ladd and W. Paul, Solid State Commun. **7**, 425 (1969).
[73] C. Neuman, A. Lawson, and R. Brown, J. Chem. Phys. **41**, 1591 (1964).
[74] T. Driscoll, H.-T. Kim, B.-G. Chae, B.-J. Kim, Y.-W. Lee, N. M. Jokerst, S. Palit, D. R. Smith, M. Di Ventra, and D. N. Basov, Science **325**, 1518 (2009).
[75] Z. Yang, C. Ko, and S. Ramanathan, Annu. Rev. Mater. Res. **41**, 337 (2011).
[76] Z. Tao, T.-R. Han, S. Mahanti, P. Duxbury, F. Yuan, C.-Y. Ruan, K. Wang, and J. Wu, Phys. Rev. Lett. **109**, 166406 (2012).
[77] V. R. Morrison, R. P. Chatelain, K. L. Tiwari, A. Hendaoui, A. Bruhacs, M. Chaker, and B. J. Siwick, Science **346**, 445 (2014).
[78] D. Wegkamp, M. Herzog, L. Xian, M. Gatti, P. Cudazzo, C. L. McGahan, R. E. Marvel, R. F. Haglund, Jr., A. Rubio, M. Wolf, and J. Stähler, Phys. Rev. Lett. **113**, 216401 (2014).
[79] E. Abreu, S. Wang, G. Ramirez, M. Liu, J. Zhang, I. K. Schuller, and R. D. Averitt, arXiv:1410.6804.